Journal of Nuclear Materials 394 (2009) 26–33

Contents lists available at ScienceDirect

Journal of Nuclear Materials

journal homepage: www.elsevier.com/locate/jnucmat

# Study of thermodynamic properties of Np–Al alloys in molten LiCl–KCl eutectic

P. Souček *, R. Malmbeck, E. Mendes, C. Nourry, D. Sedmidubský, J.-P. Glatz

*European Commission, JRC, Institute for Transuranium Elements, Postfach 2340, 76125 Karlsruhe, Germany*

ARTICLE INFO

*Article history:*
Received 3 March 2009
Accepted 4 August 2009

ABSTRACT

Pyrochemical methods are investigated worldwide within the framework of Partitioning and Transmutation concepts for spent nuclear fuel reprocessing. Electroseparation techniques in a molten LiCl–KCl are being developed in ITU to recover all actinides from a mixture with fission products. During the process, actinides are selectively electrochemically reduced on a solid aluminium cathode, forming solid actinide–aluminium alloys. This work is focused on the thermodynamic properties of Np–Al alloys in a temperature range of 400–550 °C and on the characterisation of the structure and chemical composition of deposits obtained by electrodeposition of Np on solid Al electrodes in a LiCl–KCl–$NpCl_3$ melt. Cyclic voltammetry and open circuit chronopotentiometry have been used to examine the electrochemical behaviour of Np on inert W and reactive Al electrodes. Gibbs energies, enthalpy and entropy of formation and standard electrode potentials of Np–Al alloys were evaluated and compared with *ab initio* calculations. Galvanostatic electrolyses at 450 °C were carried out to recover Np onto Al plates and the solid surface deposits were characterised by XRD and SEM-EDX analyses. Stable and dense deposits consisting of $NpAl_3$ and $NpAl_4$ alloys were identified. In addition, the conversion of $NpO_2$ to $NpCl_3$ is described, using chlorination of the oxide in a molten salt media by pure chlorine gas.

## 1. Introduction

Managing spent nuclear fuel in a safe and economic manner represents, nowadays, one of the most important issues directly connected to the sustainable development of nuclear energy. The considered strategies for the spent nuclear fuel treatment can be divided into three main areas: (i) disposal of spent fuel into deep geological repositories with no recycling, (ii) single-recycling of uranium and plutonium and (iii) a closed fuel cycle including reprocessing of all actinides. Implementation of a reactor technology with a closed fuel cycle scenario [1] is very promising not only due to the significant reduction of radiotoxicity and volume of generated spent nuclear fuel, but this concept would also save considerable uranium resources used for fabrication of the conventional fuel.

Nowadays, the reprocessing of nuclear fuels concentrates on single-recycling of uranium and plutonium. However, the major objectives for future nuclear reactor systems are an effective fuel utilization and waste minimization through recycling of all actinides. For this reason, advanced technologies for recovery of minor actinides (MA: Np, Am, Cm) together with uranium and plutonium are being developed [2]. Pyrochemical separation techniques represent a promising alternative to aqueous reprocessing processes for a group-selective recovery of actinides from spent fuel. The minor actinide-containing advanced fuels (e.g. metallic, nitride, carbide, CERMET fuels and fuels with inert matrices) might be very difficult to process by aqueous techniques due to their limited solubility.

Electrorefining [3] and liquid–liquid metal reductive extraction [4] are the most developed pyrochemical techniques designed for separation of actinides (An) from a mixture with fission products, and especially lanthanides (Ln), in a molten salt media. Processes based on both techniques have been proposed using both solid and liquid aluminium for recovery of actinides. The available activity coefficients of actinides (U, Pu) and lanthanides (Ce) in different reactive metals show that aluminium has the highest ability for a group-selective separation of all actinides [5].

An electrorefining process in a molten chloride salt medium using solid aluminium cathodes is under development in ITU. In this process, actinides dissolved in LiCl–KCl electrolyte are separated from fission products by electrolysis and selectively recovered in a form of solid actinide–aluminium (An–Al) alloys. The basic applicability of this technique for separation of actinides from lanthanides has already been demonstrated in laboratory scale. An excellent separation of actinides from lanthanides has been achieved by electrorefining of non-irradiated metallic alloy fuel composed of $U_{61}Pu_{22}Zr_{10}Am_2Nd_{3.5}Gd_{0.5}Y_{0.5}Ce_{0.5}$ [5] and also a very high capacity of aluminium to take up actinides has been experimentally proven [6,7].

The separation abilities of the electrorefining process strongly depend on the stability of the formed An–Al alloys. This work

---

* Corresponding author. Tel.: +49 (0) 7247 951124; fax: +49 (0) 7247 95199124.
*E-mail address:* Pavel.Soucek@ec.europa.eu (P. Souček).

0022-3115/$ - see front matter © 2009 Elsevier B.V. All rights reserved.
doi:10.1016/j.jnucmat.2009.08.003

has therefore been focused on the thermochemical properties of Np–Al alloys in a temperature range of 400–550 °C and on the characterisation of the structure and chemical composition of deposits obtained by electrodeposition of Np on solid Al electrodes in a LiCl–KCl–$NpCl_3$ melt. Cyclic voltammetry (CV) and open circuit chronopotentiometry (OCP) were used to examine the electrochemical behaviour of Np on inert W and reactive Al electrodes. Gibbs energies, enthalpy and entropy of formation and standard electrode potentials of Np–Al alloys were evaluated and compared with *ab initio* calculations. Galvanostatic electrolyses at 450 °C were used to recover Np onto Al plates and the deposits were characterised by XRD and SEM-EDX analyses. In addition, a conversion method of $NpO_2$ to $NpCl_3$ is described in the work, using chlorination of the oxide in a molten salt media by pure chlorine gas.

## 2. Experimental

### 2.1. Electrochemical experiments

The electrochemical experiments, storage and handling of all chemicals were carried out in a glove-box under purified Ar atmosphere (<5 ppm of water and oxygen). Electrochemical experiments and electrodeposition runs were carried out in a three-electrode set-up connected to a PAR 273 potentiostat using CorrWare2 electrochemical software. Working electrodes for CV and OCP measurements were made of W and Al wires, diameter 1 mm, dipped approximately 0.5 cm into the melt. The active electrode surface was determined by measuring the immersion depth of the electrode in the bath. A Mo wire bent into the shape of a spiral served as the auxiliary electrode and the reference electrode was an Ag/LiCl–KCl–AgCl (1 wt.%) prepared in a Pyrex glass tube. Electrodeposition of Np was performed by potentiostatic electrorefining of Np–Zr alloy melt using aluminium plate cathodes with effective areas 2.57 $cm^2$. The alloy was placed in a Ta basket in a stoichiometric excess in comparison to the desired mass of Np metal to be deposited in order to prevent Zr co-oxidation. An alumina crucible was used as a container for the molten salt. The temperature of the bath was monitored by a chromel–alumel thermocouple in an $Al_2O_3$ sheath immersed directly in the melt.

The Np concentration in the bath was followed by ICP-MS analysis of the salt samples (about 100 mg) regularly taken during the experiment. The deposits obtained by electrodeposition were characterised by SEM coupled with EDX measurements and analysed by XRD to determine the phase composition. The SEM observations were performed on a Philips XL40 SEM equipped with an EDX SD-detector. The secondary electron images and spectra were acquired with an acceleration voltage of 22 kV. The XRD analyses were carried out on a Siemens D8 advanced diffractometer in a Bragg–Brentano configuration equipped with a Ge(111) incident beam monochromator and a VANTEC position sensitive detector, using the Rietveld method for structure refinements and quantitative phase analysis.

### 2.2. Melt preparation

The melt containing dissolved neptunium was prepared by chlorination of $NpO_2$ in a LiCl–KCl eutectic melt by pure chlorine gas in a glove-box equipped with a chlorine gas line enabling transport and off-gas treatment of the used gas. A quartz reactor with a gas-tight sealed lid, having throughputs for guiding adjustable quartz inlet and outlet gas tubes, was used for the reaction. Initially, a LiCl–KCl eutectic mixture was introduced into a glassy carbon crucible together with the calculated stoichiometric mass of $NpO_2$. The crucible was placed at the bottom of the reactor, which was flushed thoroughly with purified argon gas and heated to 450 °C. For chlorination, the argon gas was switched to chlorine gas with the inlet above the melt. After increasing the temperature to 650 °C, chlorine gas was bubbled directly into the melt for 4 h. The temperature was then lowered to 450 °C and the reactor was then isolated and left overnight under a static chlorine gas atmosphere. This procedure was repeated twice. Chlorine gas was finally flushed out from the reactor by argon gas, which was introduced for 1 h directly into the melt to remove the dissolved non-reacted excess of chlorine gas. The chlorination process is summarized in Table 1.

The expected chemical reaction is a carbo-chlorination process and is described by (Eq. (1)):

$$NpO_2 + 2Cl_2 + 2C \rightarrow NpCl_4 + 2CO \qquad (1)$$

Oxygen released from the oxides is reacting with carbon from the glassy carbon crucible and forms predominantly carbon oxide. Formation of carbon dioxide and carbonyl dichloride is also expected, since the thermodynamically calculated ratios of CO:$CO_2$ and CO:$COCl_2$ in the reaction product are 1:0.11 in both cases. Besides $NpCl_4$, traces of $NpCl_3$ were formed. Although the calculated ratio $NpCl_4$:$NpCl_3$ is only 1:0.0066 at 650 °C, the electrochemical characterisation of the melt by cyclic voltammetry directly after chlorination revealed the presence of both species. In addition, these measurements showed some impurities in the melt, likely Np oxychloride compounds, formed according to (Eq. (2)).

$$NpO_2 + Cl_2 + C \rightarrow NpOCl_2 + CO \qquad (2)$$

In order to obtain pure LiCl–KCl–$NpCl_3$ electrolyte, the melt resulting from the chlorination was purified by the subsequent reduction and oxidation steps. The complete neptunium content was reduced to Np–Bi alloy by the addition of an excess of Li–Bi alloy (35 mol.% of Li) and collected in the Bi pool at the bottom of the alumina crucible. The reduced Np was then re-oxidised into the melt by addition of $BiCl_3$. The working temperature of the reduction and re-oxidation reactions was 500 °C and the bath was agitated by purified Ar gas bubbling. After completion of the reactions, the bath was frozen and the salt and Bi phases were mechanically separated from each other. The resulting melt was fully free from impurities and suitable for electrochemical investigations, as evidenced by the cyclic voltammetry characterisation (see Fig. 1).

### 2.3. Ab initio calculations

In addition to the experimental determination of thermodynamic quantities, the enthalpies of formation of three intermetallic compounds, $NpAl_2$, $NpAl_3$ and $NpAl_4$, were evaluated from total energies obtained from full potential electronic structure calculations performed using Wien2k code [8]. The augmented plane waves plus local orbitals (APW+lo) basis set expanded up to an energy cut-off of 270 eV, PBE96 parametrization scheme [9] to generalized gradient approximation (GGA) and the *k*-point mesh with a typical density 780 points $Å^3$ were employed in all calculations. The spin-polarized ground-state with spin–orbit coupling applied on scalar relativistic eigenstates in a second variation step was considered in all cases. The crystal structure data of $NpAl_2$, $NpAl_3$ and $NpAl_4$ were adopted from [10–12], respectively. The simple structures of the constituent elements, α-Al (*Fm3m*) and γ-Np (*Im3m*), were considered as reference states for the evaluation. Since γ-Np is only stable above 576 °C, its lattice parameters had to be optimised and the resulting enthalpy of formation was subsequently converted to the thermodynamic standard state referring to α-Np using the known values of $\Delta H(\alpha \rightarrow \beta) = 5.6\ kJ\ mol^{-1}$ and $\Delta H(\beta \rightarrow \gamma) = 5.3\ kJ\ mol^{-1}$.

**Table 1**
Parameters of the chlorination process for preparation of the $NpCl_3$-containing melt.

| Chlorinated material | Mass [g] | Mass LiCl–KCl [g] | Chlorination | | | Product conc. [wt%] |
|---|---|---|---|---|---|---|
| | | | Time [h] | Temperature [°C] | Technique | |
| $NpO_2$ | 1.119 | 24.925 | 8.0 | 650 | Direct bubbling into melt | 3.20 ($Np^{3+}$) |
| | | | 15 | 520 | Reactor isolated under $Cl_2$ | |

## 3. Results and discussion

### 3.1. Cyclic voltammetry

Cyclic voltammetry experiments were carried out using tungsten and aluminium working electrodes in the $NpCl_3$–LiCl–KCl salt at temperatures of 400, 450, 500 and 550 °C. Measurements on the inert tungsten electrode (see Fig. 1) revealed typical two-step reduction mechanism of $Np^{4+}$ ions to Np metal, which is in good agreement with the literature data [13,14]. $Np^{3+}$ ions are reduced to Np metal in one step involving a transfer of three electrons. The respective reduction peak ($Ep_{IIc}$) at a potential of −1.68 V vs. AgCl/Ag is associated with a sharp re-oxidation peak ($Ep_{IIa}$) at −1.49 V vs. AgCl/Ag, corresponding to the dissolution of the deposited Np metal. At more positive potentials (+0.5 V vs. AgCl/Ag), a wave with a characteristic shape for a soluble–soluble transition was detected, corresponding to the $Np^{3+}/Np^{4+}$ red-ox couple (potential values are for a temperature of 450 °C).

Using the Al working electrode (see Fig. 1, bold curve), two red-ox systems were observed. Peaks ($Ep_{Ic}$) and ($Ep_{Ia}$) at −1.21 and −0.95 V vs. AgCl/Ag, are attributed to the formation and re-oxidation of Np–Al alloy, respectively. Due to the decrease of the neptunium activity in aluminium during the alloy formation, the electrodeposition of $Np^{3+}$ on Al occurs at a more anodic potential compared to the inert W cathode. This process is referred as "underpotential deposition". A similar behaviour has been reported on Al electrodes for other actinides (U, Pu and Am [15,16]) and for several lanthanides [17–19]. The re-oxidation of Np–Al alloy is well distinguished from oxidation of pure Al electrode, in contrast to the U–Al alloys investigated in previous work [15]. The second pair of peaks ($Ep_{IIc}$ and $Ep_{IIa}$) was detected at the same potential as on the inert electrode and corresponds to the reduction of $Np^{3+}$ to Np metal.

Similar electrochemical characteristics were detected at all working temperatures for both electrode materials. An expected shift towards positive potentials was observed with increasing temperatures, as illustrated in Fig. 2 by a series of CVs measured on an Al working electrode.

### 3.2. Open circuit chronopotentiometry

The open circuit chronopotentiometry (OCP) technique was used to study the Np–Al intermetallic compounds using solid aluminium electrodes. A short electrodeposition of pure Np metal was carried out on an Al wire, followed by measurements of its open circuit potential vs. time. As the deposited Np metal reacts with aluminium forming intermetallic compounds, the relaxation $E$–$t$ curve displays potential plateaus. Although the Np–Al phase diagram is not available, three intermetallic compounds were reported by Kassner and Peterson [20]: $NpAl_2$, $NpAl_3$ and $NpAl_4$. Accordingly, five potential plateaus were expected: the most negative plateau associated with $Np^0/Np^{3+}$ red-ox couple and plateaus corresponding to the co-existence of two phases at the electrode surface in equilibrium with the dissolved $Np^{3+}$ ions (in the ascending potential sequence): Np–$NpAl_2$, $NpAl_2$–$NpAl_3$, $NpAl_3$–$NpAl_4$ and $NpAl_4$–Al. Analogous interpretation of the plateaus can be found in literature, e.g. for Ta–Ni [21] or Pd–Li [22] intermetallic compounds.

However, only 4 plateaus were detected at potentials (Np) −1.61 V, (1) −1.15 V, (2) −1.13 V and (3) −1.08 V vs. Ag/AgCl (values at 400 °C), as shown in Fig. 3. The plateau (Np) corresponds to pure Np metal deposition and it was assumed that the plateaus (1)–(3) are associated with two-phase mixtures $NpAl_2$–$NpAl_3$, $NpAl_3$–$NpAl_4$ and $NpAl_4$–Al, respectively. The Np–$NpAl_2$ plateau was not detected by the used technique, probably because the kinetic of $NpAl_2$ formation reaction is too rapid. The elimination of this plateau is sustained by the following reasons: (i) due to a huge excess of Al, the formation of Np–Al alloys on the electrode surface inevitably ends with co-existence of the most Al-rich alloy ($NpAl_4$) with Al. Therefore, the most positive plateau (3) is associated with the equilibrium $NpAl_4$–Al/$Np^{3+}$. This plateau was constant with time and close to the experimentally-determined rest potential of pure Al electrode (−1.06 V vs. Ag/AgCl at 400 °C). (ii) According to the published Gibbs energy of formation for $PuAl_2$ [23], which has the same cubic crystallographic structure as $NpAl_2$, the

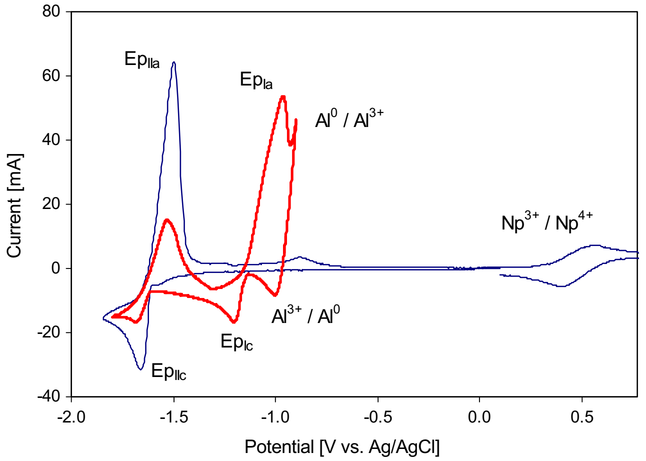

**Fig. 1.** CVs of LiCl–KCl–$NpCl_3$ ($[Np^{3+}]$ = 3.20 wt.%) on W and Al (bold line) working electrodes at 450 °C, scan rate 100 mV $s^{-1}$.

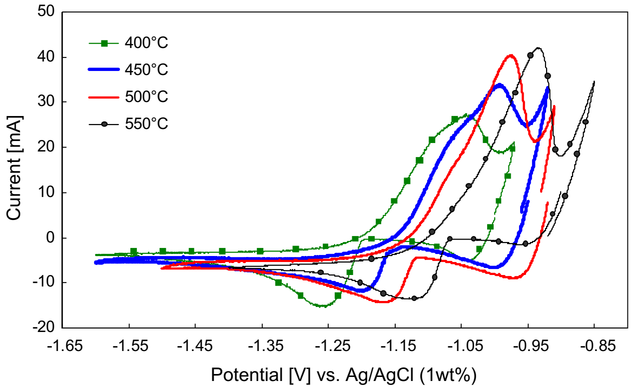

**Fig. 2.** A comparison of CVs recorded on a solid Al working electrode in LiCl–KCl–$NpCl_3$ ($[Np^{3+}]$ = 3.20 wt.%) at temperatures 400–550 °C, scan rate 100 mV $s^{-1}$.

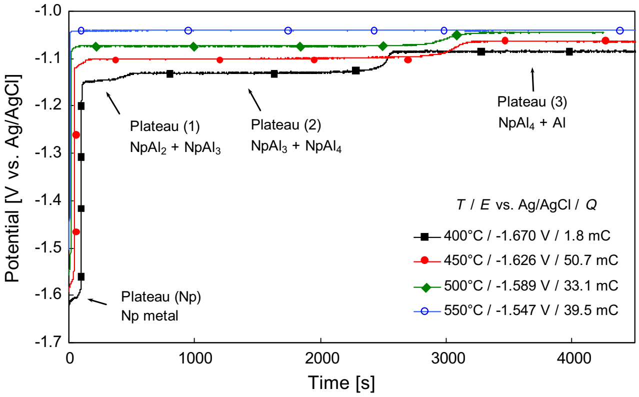

**Fig. 3.** Comparison of OCP curves measured on Al solid electrode in LiCl–KCl–$NpCl_3$ ($[Np^{3+}]$ = 3.20 wt.%) at temperatures *T* from 400 to 550 °C. *E* = pre-deposition potential, *Q* = charge passed during the pre-deposition.

Np–$NpAl_2$ plateau should be expected at more negative potentials than plateau (1).

The plateaus can be described by the following electrochemical reactions (Eqs. (3)–(6)):

$$\text{Plateau (Np)}: \quad Np^0 \leftrightarrow Np^{3+} + 3e^- \tag{3}$$

$$\text{Plateau (1)}: \quad 3NpAl_2 \leftrightarrow Np^{3+} + 3e^- + 2NpAl_3 \tag{4}$$

$$\text{Plateau (2)}: \quad 4NpAl_3 \leftrightarrow Np^{3+} + 3e^- + 3NpAl_4 \tag{5}$$

$$\text{Plateau (3)}: \quad NpAl_4 \leftrightarrow Np^{3+} + 3e^- + 4Al \tag{6}$$

Several series of OCP measurements were carried out at 400, 450, 500 and 550 °C using electrodes with fresh surfaces and with surfaces covered with pre-deposited layers of Np–Al alloys. The different behaviour on both types of surfaces is illustrated in Fig. 4. If the *E*–*t* curve was measured on clean Al surfaces at temperatures of 450 °C or higher, the potential plateau (1) was not possible to clearly distinguish. On the other hand, both plateaus (1) and (2) were identified using electrodes with pre-deposited Np–Al. These results were reproducible enough to enable a characterisation of all intermetallic compounds at all working temperatures. At 400 °C, all plateaus were detected for both surface types, which might indicate a higher stability of more Np-rich alloy at lower temperatures and/or faster diffusion of Np and Al through Np–Al alloy layer at higher temperatures.

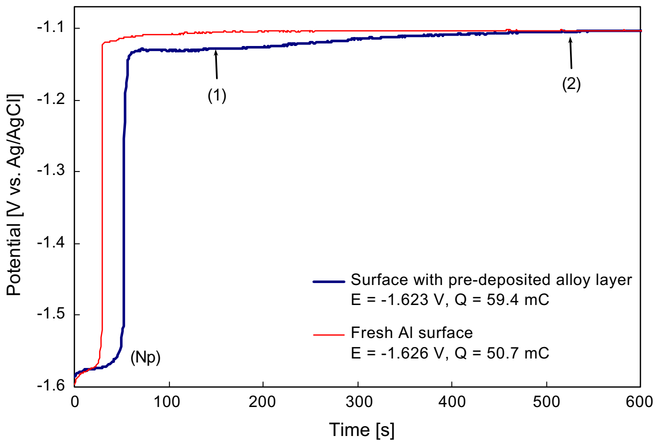

**Fig. 4.** Comparison of OCP curves measured at 450 °C on a fresh clean Al surface and on an Al surface covered with a pre-deposited layer of Np–Al alloys (thick line). *E* = pre-deposition potential vs. Ag/AgCl, *Q* = charge passed during the pre-deposition.

### 3.3. Evaluation of thermodynamic properties

The thermodynamic properties were evaluated from the experimental data obtained in the OCP measurements. The electromotive forces $\xi_1$–$\xi_3$ between Np–Al intermetallic compounds and Np metal were determined as differences between potentials of Np–Al plateaus and potential corresponding to $Np^{3+}/Np$ red-ox couple. The relaxation potential of the latter had an increasing slope on Al electrode, which indicates a partial solubility of Np in Al. Similar OCP measurements were carried out on inert W electrodes and stable potential plateaus were observed after pre-depositions of Np metal at all temperatures. These potentials are attributed to the most stable Np allotropic form at working temperatures (β-Np, *P4/nmm*, in all cases) and they were considered as reference values for the evaluation of thermodynamic properties.

The obtained electromotive forces associated with the following equilibriums (Eqs. (7)–(9)) are summarized in Table 2.

$$\xi_1 \approx (\text{Eq. 4}) - (\text{Eq. 3}) = 3NpAl_2 \leftrightarrow 2NpAl_3 + Np \tag{7}$$

$$\xi_2 (\text{Eq. 5}) - (\text{Eq. 3}) = 4NpAl_3 \leftrightarrow 3NpAl_4 + Np \tag{8}$$

$$\xi_3 (\text{Eq. 6}) - (\text{Eq. 3}) = NpAl_4 \leftrightarrow 4Al + Np \tag{9}$$

The corresponding changes of Gibbs energies, $\Delta G_i$, can be calculated from (Eq. (10)):

$$\Delta G_i = -3F\xi_i \tag{10}$$

According to (Eq. (9)), $\Delta G_3$ is equivalent directly to the Gibbs energy of formation of $NpAl_4$, $\Delta_f G(NpAl_4)$. The Gibbs energies of formation of $NpAl_2$, $\Delta_f G(NpAl_2)$, and $NpAl_3$, $\Delta_f G(NpAl_3)$ can be calculated by linear combinations of $\Delta G_i$ according to (Eqs. (11) and (12)). The linear combinations were deduced from (Eqs. (7)–(9)) to give the chemical equilibrium (Eq. (13)).

$$\Delta_f G(NpAl_3) = \frac{3\Delta G_3 + \Delta G_2}{4} \tag{11}$$

$$\Delta_f G(NpAl_2) = \frac{3\Delta G_3 + \Delta G_2 + 2\Delta G_1}{6} \tag{12}$$

$$Np + n\,Al = NpAl_n (n = 2, 3) \tag{13}$$

Series of experiments were carried out at each temperature to verify the reproducibility of the measurements (between 4 and 10 *E*–*t* curves). Both the electromotive forces $\xi$ and the Gibbs energies of formation $\Delta_f G(NpAl_n)$ are presented in Table 2 as the mean average values, followed by the standard deviations given in brackets as $1\sigma$. The plots of $\Delta_f G(NpAl_n)$ vs. *T* are shown in Fig. 5.

From the sets of $\Delta_f G(NpAl_n)$ calculated for each working temperature *T*, the enthalpies $\Delta_f H(NpAl_n)$ and entropies $\Delta_f S(NpAl_n)$ of formation were assessed by the least squares method according to the Gibbs–Helmholtz equation (Eq. (14)).

$$\Delta_f G = \Delta_f H - T \cdot \Delta_f S \tag{14}$$

under the assumption of constant values of both quantities in the given temperature interval 400–550 °C. The obtained data are given in Table 3 along with the enthalpies of formation calculated by the APW + lo method.

Since no other experimental data are available for thermodynamic properties of Np–Al intermetallic compounds, the direct comparison of the determined values is impossible. The interpolation between the isostructural U–Al and Pu–Al intermetallic compounds would predict less exothermic values of enthalpies of formation and also less negative entropies of formation which, however, refer to different structures of An-metals. The calculated enthalpies of formation are also much more endothermic compared to the experimental values. It should be noted, however, that the experimental and calculated values of $\Delta_f H$ given in Table 3 can not be compared directly, as they refer to a different state, β-Np

**Table 2**
Summary of experimentally determined thermodynamic properties of $NpAl_3$ and $NpAl_4$ alloys. Uncertainties are given in brackets as $1\sigma$.

| $T$ [°C] | $\xi_1$ [mV] | $\xi_2$ [mV] | $\xi_3$ [mV] | $\Delta_f G(NpAl_2)$ [kJ mol$^{-1}$] | $\Delta_f G(NpAl_3)$ [kJ mol$^{-1}$] | $\Delta_f G(NpAl_4)$ [kJ mol$^{-1}$] |
|---|---|---|---|---|---|---|
| 400 | 463 (3) | 480 (3) | 526 (6) | −143.90 (1.35) | −148.80 (1.65) | −152.11 (1.87) |
| 450 | 450 (2) | 476 (1) | 512 (1) | −140.43 (0.37) | −145.51 (0.24) | −148.06 (0.20) |
| 500 | 441 (4) | 475 (1) | 505 (10) | −138.54 (1.81) | −143.97 (2.20) | −146.15 (2.83) |
| 550 | 435 (2) | 473 (2) | 490 (2) | −135.66 (0.59) | −140.51 (0.55) | −141.69 (0.61) |

and α-Np, respectively, and a different temperature as well. Nevertheless, the enthalpy of transformation from β-Np to α-Np amounts only −5.6 kJ mol$^{-1}$ and the difference in heat capacity between the given intermetallic phase and the weighted sum of elements, $\Delta C_p$, is estimated to contribute (based on heat capacity of $NpAl_n$ calculated by direct method [27]) by ∼ −5–−15 kJ mol$^{-1}$. Furthermore, the calculations performed on analogous series, $UAl_n$ and $PuAl_n$, [24] turned out to be underestimated by ∼−6–−34 kJ mol$^{-1}$ compared to calorimetry data [25,26] (except for $PuAl_2$ whose stability was overestimated by 17 kJ mol$^{-1}$ compared to experiment). This calculation error might be due to higher order correlation effects acting on An-5*f* electrons which are not considered within the used GGA method. Considering all these corrections we come up to approximate values of $\Delta_f H_{673-823}$ −125, −155, −155 kJ mol$^{-1}$ for $NpAl_2$, $NpAl_3$ and $NpAl_4$, respectively, which are still ∼30–55 kJ mol$^{-1}$ less negative than the experimental data. It is noteworthy that a similar difference between the high temperature emf data [27] and ambient temperature calorimetry results [25] is observed in the case of $UAl_n$ series and can be explained in terms of a negative $\Delta C_p$ difference, which also gives rise to more negative entropies of formation at elevated temperatures compared to room temperature. Similarly, the entropies of formation $\Delta_f S_{298}$ of $NpAl_n$ assessed from low temperature heat capacities calculated *ab initio* are close to zero [24] and the $\Delta C_p$ correction as applied for enthalpies accounts only for a difference ∼−10–−25 J mol$^{-1}$ K$^{-1}$, which is still less negative than the values of $\Delta_f S_{673-823}$ given in Table 3. The reason for the observed differences in both $\Delta_f H$ and $\Delta_f S$ might lie in poorly defined tabulated data for heat capacity of $NpAl_n$, α-Np and particularly β-Np, the latter being considered as constant and only interpolated between β-U and δ′-Pu [28]. Further independent experiments such as vapour pressure measurements or dissolution calorimetry as well as high temperature heat capacity data are thus needed to clarify this discrepancy.

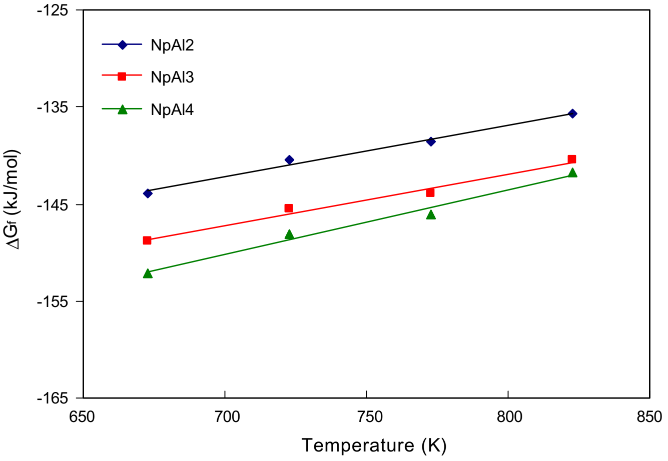

**Fig. 5.** Dependency of Gibbs energies of formation of Np–Al intermetallic compounds on temperature.

**Table 3**
Experimentally determined enthalpies and entropies of formation (referred to β-Np) for the temperature range 400–550 °C and the enthalpies of formation $\Delta_f H_0$ (referred to α-Np) assessed from ground-state total energies calculated *ab initio*.

| Phase | $\Delta_f H_{673-823}$ [kJ mol$^{-1}$] | $\Delta_f S_{673-823}$ [J mol$^{-1}$ K$^{-1}$] | $\Delta_f H_0$ [kJ mol$^{-1}$] |
|---|---|---|---|
| $NpAl_2$ | −179.4 (±2.3) | −53.2 (±1.7) | −110.2 |
| $NpAl_3$ | −184.2 (±3.2) | −52.9 (±2.7) | −122.9 |
| $NpAl_4$ | −196.6 (±3.1) | −66.3 (±2.2) | −105.6 |

### 3.4. Calculation of the alloys formation potential

For comparison of potentials corresponding to formation of Np–Al intermetallic compounds with other An–Al and Ln–Al alloys, the $Np^{3+}/NpAl_n$ standard electrode potential $E^0(Np^{3+}/NpAl_n)$ can be calculated according to the following procedure. The potential of the $NpAl_n$ plateau is defined by (Eq. (15)):

$$E(Np^{3+}/NpAl_n) = E^0(Np^{3+}/NpAl_n) + \frac{RT}{3F}\ln a(Np^{3+}) \tag{15}$$

$E^0(Np^{3+}/NpAl_n)$ can be expressed in terms of standard $Np^{3+}/Np^0$ potential, $E^0(Np^{3+}/Np^0)$, and the activity of Np in $NpAl_n$, $a_{Np}^{NpAl_n}$, according to the (Eq. (16)):

$$E^0(Np^{3+}/NpAl_n) = E^0(Np^{3+}/Np^0) - \frac{RT}{3F}\ln a_{Np}^{NpAl_n} \tag{16}$$

The term RT ln $a_{Np}^{NpAl_n}$ is equal to the above-calculated Gibbs formation energy of $NpAl_n$, $G_f(NpAl_n)$, and $E^0(Np^{3+}/NpAl_n)$ can be calculated from the following expression (Eq. (17)):

$$E^0(Np^{3+}/NpAl_n) = E^0(Np^{3+}/Np^0) - \frac{\Delta G_f(NpAl_n)}{3F} \tag{17}$$

Since $NpCl_3$ in its crystalline form was used as the reference state for $Np^{3+}$ in the melt, $E^0(NpCl_3/Np^0) = E^0(Np^{3+}/Np^0)$ and its value was calculated using data from the material property data base for *f*-elements and compounds [29].

$$E^0(NpCl_3/Np^0) = -3.095 + 7.5\cdot 10^{-4}\,T\ (V\,vs.\ Cl_2/Cl^-) \tag{18}$$

Using (Eqs. (17) and (18)), the variation of $E^0(Np^{3+}/NpAl_n)$ was determined vs. the temperature and the values were recalculated vs. the used AgCl/Ag reference electrode according to the procedure described in [30].

$$E^0(Np^{3+}/NpAl_2) = -1.3872 + 7.5148\cdot 10^{-4}\,T \tag{19}$$

$$E^0(Np^{3+}/NpAl_3) = -1.3699 + 7.5252\cdot 10^{-4}\,T \tag{20}$$

$$E^0(Np^{3+}/NpAl_4) = -1.3284 + 7.0623\cdot 10^{-4}\,T \tag{21}$$

### 3.5. Electrodeposition of Np–Al alloys

Two potentiostatic electrodeposition runs in the LiCl–KCl–$NpCl_3$ melt were carried out on Al plates at potentials −1.20 and −1.50 V vs. AgCl/Ag at 450 °C. A relatively large potential difference was used for the runs in order to investigate the influence of the deposition potential on the composition of the deposit. Aluminium plates with effective (immersed) dimensions 12 × 10 × 0.5 mm were used as cathodes and Np–Zr alloy (79.5 wt.% Np, 0.8 g) was connected as an anode during both runs. The expected electrode reactions were selective anodic dissolution

**Table 4**
Mass balance of the electrodeposition of Np on Al electrodes and composition of deposits.

| Run | $E$ [V] | $Q$ [C] | $m_{th}$ [mg] | $m_{ex}$ [mg] | $R$ [%] | XRD analyses [wt%] | |
|---|---|---|---|---|---|---|---|
| | | | | | | $NpAl_3$ | $NpAl_4$ |
| NpAl_1 | −1.20 | 184 | 150.3 | 157.2 | 104.6 | 64.3 | 35.7 |
| NpAl_2 | −1.50 | 305 | 249.7 | 210.2 | 84.2 | 87.2 | 12.8 |

of Np from the Np–Zr alloy and reduction of $Np^{3+}$ ions forming Np–Al alloys on the cathode according to the electrochemical reactions (Eqs. (22) and (23)):

$$\text{Anodic side} \quad \mathrm{Np}_x^0\mathrm{Zr}_y \rightarrow \mathrm{Np}^{3+} + 3\mathrm{e}^- + \mathrm{Np}_{x-1}^0\mathrm{Zr}_y \tag{22}$$

$$\text{Cathodic side} \quad \mathrm{Np}^{3+} + 3\mathrm{e}^- + n\mathrm{Al} \rightarrow \mathrm{Np}^0\mathrm{Al}_n \tag{23}$$

After the electrodepositions, the electrodes were left above the salt at the working temperature for several hours in order to let the adhered melt drip down. In addition, both electrodes were then thoroughly washed in ethanol with traces of water. The basic characteristics of the runs and the mass balance evaluation are summarized in Table 4, where $E$ is the potential applied vs. AgCl/Ag, $Q$ is the charge transferred, $m_{th}$ is the theoretically calculated mass of the deposit (according to Faraday's law and assuming 100% current efficiency), $m_{ex}$ is the experimentally determined mass of the deposit (weight difference of the electrode before and after the experiment) and $R$ is the calculated overall efficiency of the process according to the (Eq. (24)):

$$R = 100 \cdot \frac{m_{ex}}{m_{th}} \tag{24}$$

Since some salt remained on the deposits, the calculated efficiency of the process exceeded 100% in case of run NpAl_1.

### 3.6. Characterisation of the Np–Al alloys

Electrodes, after electrodepositions, had homogeneously distributed shiny metallic surface deposits. After removal of the adhered salt, the electrodes were cut and divided in two pieces. One part was selected for SEM-EDX analysis, embedded in resin and surface polished. The deposit on the remaining piece was scraped off and used for XRD analysis.

The phase composition of the formed alloys was based mainly on the XRD analysis. Mixtures of $NpAl_3$ and $NpAl_4$ alloys were identified in both deposits and a significantly higher content of $NpAl_3$ alloy was detected in the run NpAl_2. The $NpAl_3/NpAl_4$ ratio was approx. 7 for NpAl_2, compared to approx. 2 for NpAl_1 (see Table 4). This indicates that more neptunium-rich alloy is formed in greater proportion at more negative potentials. Both samples contained a detectable content of KCl/LiCl originating from the residual salt, which was not fully washed out. However, an exact quantification of the salt content was not possible. The results are summarized in Table 4 and the XRD pattern for the run NpAl_2 is shown in Fig. 6.

Deposits from both electrodes were further characterised by SEM-EDX analysis. The mapping of selected regions revealed homogeneous distributions of Np and Al in the deposits along with traces of K, Li and Cl from the salt. It showed that only Np–Al alloys were formed during the electrodepositions.

EDX analyses were performed for 20 spots (10 for each electrode) selected at various heights of the electrodes and at different distances from the aluminium surfaces. The results are plotted in Fig. 7. The evaluated compositions do not exactly agree with the alloy mixtures analysed by XRD, since the Al/Np ratios determined by EDX were 2.99 for NpAl_1 and 2.87 for NpAl_2. The EDX analyser was used without direct calibration (i.e. without using $NpAl_3$ and $NpAl_4$ as standards). Moreover, the EDX analyser gives average values from the excited volume and therefore may include areas of different compositions not visible on the surface. The results obtained by XRD and SEM-EDX were therefore considered to be con-

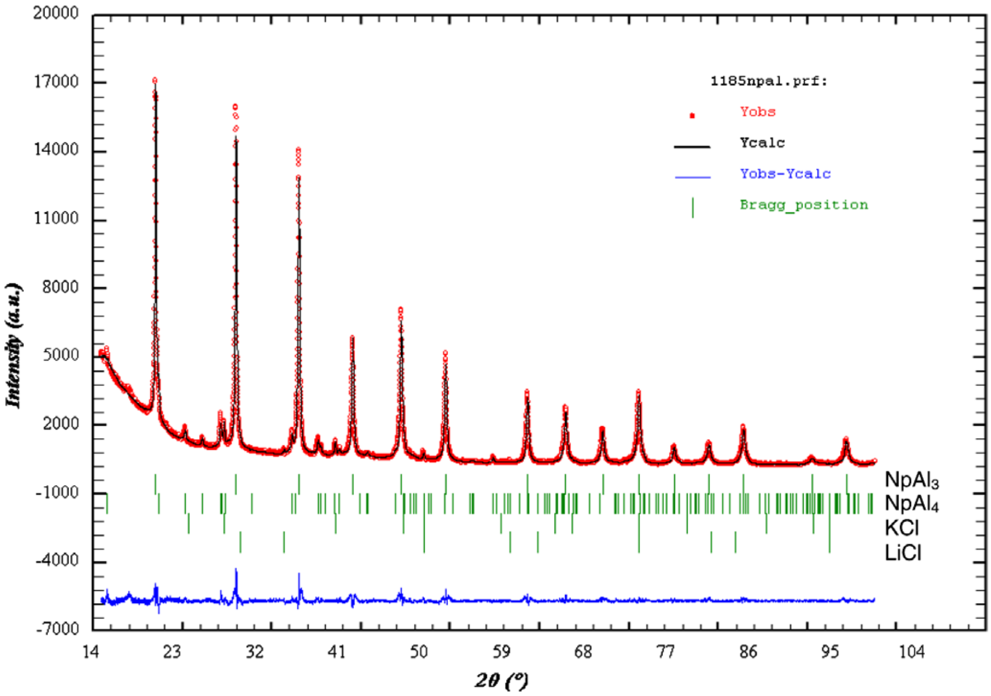

**Fig. 6.** XRD pattern of the deposit from run NpAl_2. The ticks correspond to the Bragg positions for $NpAl_3$, $NpAl_4$, KCl and LiCl (in a descending order).

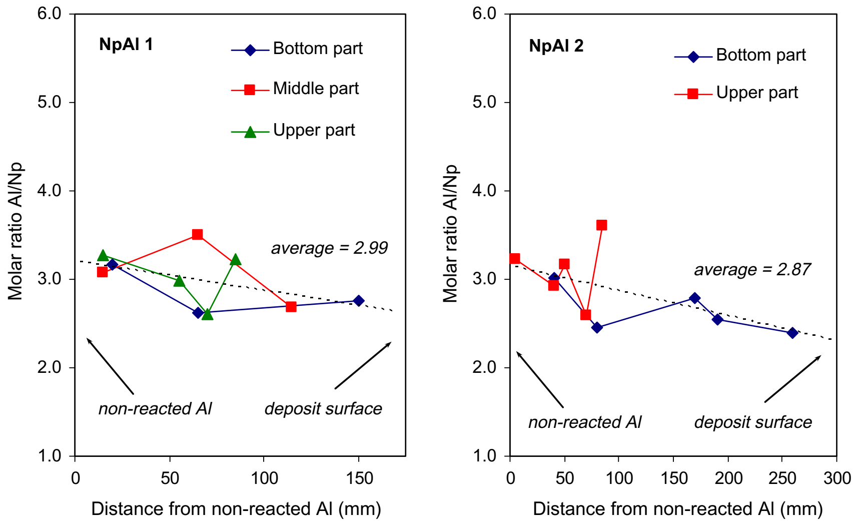

**Fig. 7.** SEM-EDX determinations of the molar ratio Al/Np vs. the distance from the aluminium surface for the electrode from run NpAl_1 (left) and NpAl_2 (right).

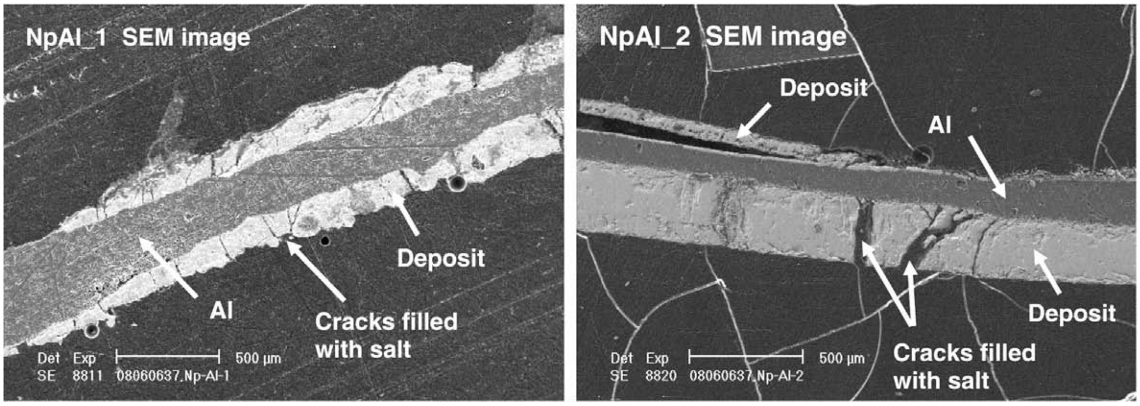

**Fig. 8.** SEM micrographs of the electrode from run NpAl_1 (left, magnification 45×) and NpAl_2 (right, magnification 50×), white lines on the right picture are cracks in the resin originating from the sample preparation.

sistent. The more neptunium-rich alloy mixture was identified by EDX at more negative deposition potential, which is in agreement with the XRD results. The compositions of the spots are relatively regularly distributed around the average values and no direct evidence for formation of more Al-rich alloys at the centre of the electrode can be assessed from the analysis. Nevertheless there is a slight fall in Al/Np ratio with distance from non-reacted Al surface (see Fig. 7) and this would be expected given the deposition of Np at the alloy/solution interface.

Relatively dense deposits composed mainly of monolithic blocks of the alloy were obtained in both cases, as evidenced by selected SEM micrographs shown in Fig. 8. The Np–Al alloy region is quite distinct from that of the Al cathode. Nevertheless the Np–Al alloy appears to be adherent to the Al cathode. Even the deposit in NpAl_2 is splitting off within the Np–Al deposit. The distribution of the deposit is not uniform on the sides of the NpAl_2 electrode, as one side was probably positioned too close to the crucible wall and yielded an irregular electric field. Average thicknesses of the Np–Al layers were 160 µm for NpAl_1 and 290 µm for NpAl_2. The cracks in between the alloy blocks are filled with salt, which was proved by the EDX analysis of the respective spots. However, at certain regions of the electrodes, a more porous deposit was formed with spherical salt-filled spaces.

## 4. Conclusions

The electrochemical behaviour of Np in molten LiCl–KCl has been investigated using inert tungsten and reactive aluminium electrodes at temperatures from 400 to 550 °C. The phenomenon referred to as “underpotential deposition” has been observed on Al electrodes, that is the formation of Np–Al alloys has been detected at more positive potentials than the reduction to the pure actinide metal. Cyclic voltammetry and open circuit chronopotentiometry techniques have been used to determine deposition potentials and Gibbs energies, enthalpies and entropies of formation for the intermetallic compounds $NpAl_2$, $NpAl_3$ and $NpAl_4$. The enthalpies of formation determined from the EMF measurements have been compared with those calculated from the first principles. More endothermic values were found by the latter approach.

The chemical composition, structure and distribution of the Np–Al alloys formed during the electrodeposition process have been investigated by XRD and SEM-EDX analyses. Neptunium has been electrodeposited on aluminium plates using potentiostatic technique. The analyses have revealed mixtures of $NpAl_3$ and $NpAl_4$ alloys as the major constituents of the deposits with $NpAl_3$ identified as a major component. The composition of the deposit is influenced by the applied deposition potential and by the operation period of the process. More neptunium-rich alloys have been detected using more negative deposition potentials, while the inter-diffusion during the process is expected to enhance the formation of more aluminium rich alloys. Since these effects – deposition potential and diffusion time – act in opposing directions, it was impossible to explicitly assess their influence on the deposit composition with these experiments. Consequently, the analysis of the deposits obtained from relatively long-term electrodepositions may not correspond to the chemical composition of the alloys, which are formed by short-term polarization during the OCP experiments.

The structures of the deposits have been evaluated on the basis of the SEM analyses. Dense and regularly distributed deposits with only small cracks filled with salt have been observed. EDX mappings have confirmed formation of homogeneous Np–Al alloys directly after the Np metal has deposited.

## Acknowledgements

The authors wish to thank R. Jardin for XRD measurement and evaluation, T. Wiss and H. Thiele for SEM-EDX analyses, M. Cardinale and S.v. Winckel for ICP-MS analysis as well as M. Ougier and A. Rodrigues for experimental support. This work was carried out with European Commission financial support in the 7th Framework programme, under the contract 211267 “ACSEPT”.

## References

[1] A Technology Roadmap for Generation IV Nuclear Energy Systems, US DOE Nuclear Energy Research Advisory Committee at the Generation IV International Forum, GIF-002-00, 2002, available online: <http://gif.inel.gov/roadmap/>.
[2] Actinide and Fission Product Partitioning and Transmutation – Status and Assessment Report, OECD-NEA, 1999, available online: <http://www.nea.fr/html/trw/docs/neastatus99/completedoc.pdf>.
[3] J.J. Laidler et al., Progress in Nuclear Energy 31 (1/2) (1997) 131–140.
[4] K. Kinoshita et al., Journal of Nuclear Science and Technology 36 (2) (1999) 189–1979.
[5] O. Conocar et al., Nuclear Science and Engineering 153 (2006) 253–261.
[6] L. Cassayre et al., Journal of Nuclear Materials 360 (2007) 49–57.
[7] P. Souček et al., Radiochimica Acta 96 (2008) 315–322.
[8] P. Blaha et al., WIEN2k, An Augmented Plane Wave + Local Orbitals Program for Calculating Crystal Properties, Karlheinz Schwarz, Techn. Universität Wien, Austria, 2001, ISBN 3-9501031-1-2.
[9] J.P. Perdew, S. Burke, M. Ernzerhof, Physical Review Letters 77 (18) (1996) 3865–3868.
[10] A.T. Aldred et al., Physical Review B 10 (3) (1974) 1011–1019.
[11] A.W. Mitchell, D.J. Lam, Journal of Nuclear Materials 52 (1) (1974) 125–127.
[12] O.J.C. Runnalls, Transactions of the American Institute of Mining, Metallurgical and Petroleum Engineers 197 (1953) 1460–1472.
[13] P. Masset et al., Journal of Electroanalytical Chemistry 603 (2007) 166–174.
[14] P. Masset et al., Journal of Nuclear Materials 344 (2005) 173–179.
[15] L. Cassayre et al., Journal of Nuclear Materials 378 (2008) 79–85.
[16] J. Serp et al., Journal of the Electrochemical Society 152 (2005) C167.
[17] Y. Castrillejo et al., Electrochimica Acta 51 (2006) 1941–1951.
[18] Y. Castrillejo et al., Electrochimica Acta 50 (2005) 2047–2057.
[19] Y. Castrillejo et al., Journal of Electroanalytical Chemistry 575 (2005) 61–74.
[20] M.E. Kassner, D.E. Peterson, Bulletin of Alloy Phase Diagrams 10 (2) (1989) 111–112.
[21] P. Taxil, Journal of the Less-Common Metals 113 (1985) 89–101 (in French).
[22] T. Nohira, Y. Ito, Journal of the Electrochemical Society 145 (3) (1998) 785–790.
[23] M.E. Kassner, D.E. Peterson, Bulletin of Alloy Phase Diagrams 10 (4a) (1989) 459–465.
[24] D. Sedmidubský, P. Souček, R.J.M. Konings, Journal of Nuclear Materials, JNM-D-09-00307, submitted for publication.
[25] M.I. Ivanov, V.A. Tumbakov, N.S. Podolskaya, Atomnaya Energiya 5 (1958) 166–170 (in Russian).
[26] V.V. Akhachinski et al., Heat of formation of intermetallic compounds of plutonium with aluminium and iron and of uranium with iron, in: Thermodynamics of Nuclear Materials – Proc. Int. Symp. Vienna, IAEA, 1962.
[27] V.A. Lebedev et al., Russian Journal of Atomic Energy 32 (2) (1972) 115–118 (in Russian).
[28] R. Guillaumont et al., Chemical Thermodynamics Vol. 5: Update on the Chemical Thermodynamics of Uranium, Neptunium, Plutonium, Americium and Technetium, Elsevier, Amsterdam, 2003.
[29] The ITU Material Property Data Base for f-Elements and Compounds, f-MPD: <http://itu.jrc.ec.europa.eu/index.php?id=405>.
[30] S.P. Fusselman et al., Journal of the Electrochemical Society 146 (7) (1999) 2573.